scientific reports

Check for updates

OPEN

Reactive co-sputtered Li–Nb–O thin films with tunable ionic conductivity and dielectric properties for energy storage applications

Samaneh Jafarpour[1], Hamid Naghshara[1,2]✉ & Hamaneh Zarenezhad[3]

Lithium niobate ($LiNbO_3$) has emerged as a promising solid-state electrolyte for energy storage systems owing to its favorable ionic conductivity and distinctive physicochemical properties. However, conventional solution-based synthesis routes are limited by Li loss, compromising performance. This study reports for the first time the development of Li–Nb–O thin films using reactive magnetron co-sputtering of Nb and Li targets at various DC powers and constant RF power. This approach yields the growth of amorphous films at room temperature, as confirmed by X-ray diffraction. Morphological studies revealed that increasing DC power promotes grain growth. EDX analysis indicated a rise in Nb/O atomic ratio from 0.28 to 0.44 with increasing DC power (20–80 W). XPS experiments provided evidence supporting the dominant presence of Nb-oxygen bonds and a growing contribution from weakly bound Li species at higher Nb concentrations. Moreover, the Li-to-Nb atomic ratio was found to range from 2.31 to 1.36 with increasing DC power (20–80 W), corroborating the formation of a Li-rich compositional region. Temperature-dependent impedance spectroscopy demonstrated enhanced ionic diffusion in Li–Nb–O films with higher Nb content, attributed to a reduction in activation energy. The highest room-temperature ionic conductivity of co-sputtered films reached 1.33×10^{-7} S cm^{-1}. Metal–insulator-metal capacitors based on the optimized Li–Nb–O thin films exhibited a high capacitance (~ 624.86 nF cm^{-2}), a large dielectric constant (~ 141.21), and a low loss tangent. In this way, a electric double layer was formed at the electrolyte/electrode interfaces. These findings underscore the potential of reactive co-sputtered Li–Nb–O films as solid-state electrolytes for energy/charge storage applications.

Keywords Lithium niobate, Solid-state electrolyte, Energy storage, Magnetron co-sputtering, Ionic conductivity, Capacitors

In recent years, miniaturized energy storage devices with high power density have garnered significant attention due to their critical role in powering portable, wearable, and implantable electronics[1]. The evolution of microelectronic products, such as smart devices, MEMS, microrobots, sensors, RFID tags, and biomedical implants, has intensified the demand for miniaturized energy storage devices[2]. Lithium-ion batteries (LIBs) and supercapacitors are widely studied as efficient, reliable power sources for the consumer electronics and electric vehicles (EVs)[3,4].

Miniaturization of commercial LIBs and supercapacitors with flammable liquid electrolytes is restricted by multiple factors, including design, size, shape, and integrity. Further limitations arise from reduced flexibility, safety concerns, leakage risk, processing costs, and lifespan[5]. To address these challenges, solid-state electrolytes (SSEs) have been proposed as promising alternatives to conventional liquid electrolytes[6].

The most popular Li-ion conductors include nitrides (Li_3N)[7], oxynitrides (LiPON)[8], NASICON-type ($Li_{1.3}Al_{0.3}Ti_{1.7}(PO_4)_3$)[9], perovskites ($Li_{3x}La_{2/3-x}TiO_3$)[10], and garnets ($Li_7La_3Zr_2O_{12}$)[11]. In addition, sulfides

[1]Faculty of Physics, University of Tabriz, Tabriz, Iran. [2]Research Institute of Applied Physics and Astronomy, University of Tabriz, Tabriz, Iran. [3]Koç University Surface Science and Technology Center (KUYTAM), Istanbul, Turkey. ✉email: naghshara@tabrizu.ac.ir

($Li_{10}GeP_2S_{12}$)[12], hydrides ($Li_2B_{12}H_{12}$)[13], and halides ($LiAlCl_4$)[14] represent important classes of Li-ion conductors. The implementation of specific SSEs in energy storage is constrained by low power density. This limitation arises from poor ionic conductivity and high interfacial resistance to Li-ion transport[15].

Amorphous thin-film SSEs offer a promising approach to overcome low ionic conductivity and enable compact device integration[16]. Thin-film electrolytes can reduce contact resistance, often by 1–2 orders of magnitude. This improvement arises from reduced interfacial defects, stronger chemical bonding with bulk materials, and effective filling of voids[17]. Extensive efforts have been dedicated to advancing thin-film processing compatible with micro- or nanofabrication of power storage devices[18]. Thin-film deposition of various solid-state electrolytes (SSEs) has been extensively reported in the literature. Examples include Li_3PO_4[19], $LiAlO_2$[20], Li_xTaO_y[21], $Li_{1+x}Al_xGe_{2-x}(PO_4)_3$[22], Li–Al–Ti–P–O–N[23], and Li_3InCl_6[24].

Beyond these, lithium niobate ($LiNbO_3$) has gained attention as a multifunctional material for use in the Li-ion batteries[25], transistors[26], and electrochromic displays[27]. It is also employed in wave transducers[28], electro-optic modulators[29], waveguides[30], and Q-switches[31]. Crystalline lithium niobate is well known for its unique properties, including ferroelectricity, piezoelectricity, pyroelectricity, and electrochromism. In addition, $LiNbO_3$ exhibits acousto-optic interactions, photoelasticity, and photovoltaic effects[32]. Amorphous $LiNbO_3$ exhibits high ionic conductivity owing to its structural disorder, making it a promising solid-state electrolyte. Ferroelectric $LiNbO_3$ films demonstrate dielectric-like behavior in amorphous state[33]. Several studies report room-temperature ionic conductivities of $LiNbO_3$ up to 10^{-5} S cm^{-1} for the glassy (amorphous) form, and 10^{-9}–10^{-7} S cm^{-1} for the crystalline counterpart[34].

$LiNbO_3$ thin films have been deposited via various techniques, inclusing sol–gel[35], chemical vapor deposition (CVD)[36], epitaxial growth by melting (EGM)[37], and molecular beam epitaxy (MBE)[38]. Other methods include pulsed laser deposition (PLD)[39], atomic layer deposition (ALD)[40], and magnetron sputtering[41]. Solution-based chemical methods typically require heat treatment to eliminate residual solvents. These processes in Li-containing film deposition is hindered by challenges such as Li loss, void formation, and thermal-stress-induced cracking. Notably, these issues arise even at moderate temperatures (400–600 °C)[42]. Pulsed laser deposition (PLD) is unsuitable for the industrial applications and mass production due to limited film area (~ 1 cm^2)[43].

Magnetron sputtering constitutes a viable and robust technique in the microelectronics, offering room-temperature fabrication of thin films with uniform thickness, high purity, and strong substrate adhesion. It also enables tunable composition and scalability from laboratory research to industrial production[44,45]. Generally, radio-frequency (RF) sputtering of ceramic targets is used for the deposition of Li-containing thin films, such as Li_2MnO_3[46], $LiNbO_3$[47], and $Li_7La_3Zr_2O_{12}$[48].

In this work, we report for the first time the synthesis of Li–Nb–O films via co-sputtering of niobium (Nb) and lithium (Li) targets in a reactive oxygen atmosphere. This approach allows precise control over the Li content, with the Li target serving as an independent and primary Li source. This study investigates the influence of co-sputtering parameters on the crystallinity, grain growth, elemental distribution, and oxidation states of Li–Nb–O films. Particular attention is given to the effect of deposition conditions on their ionic transport and dielectric performance. These analyses explore the potential of Li–Nb–O thin films as solid-state electrolytes for next-generation energy storage applications.

Experimental section

Thin film deposition

Li–Nb–O thin films were deposited at room temperature using a reactive magnetron co-sputtering system (MECA-2000), as illustrated in Fig. 1. Glass substrates were cleaned sequentially in acetone, ethanosl, and DI

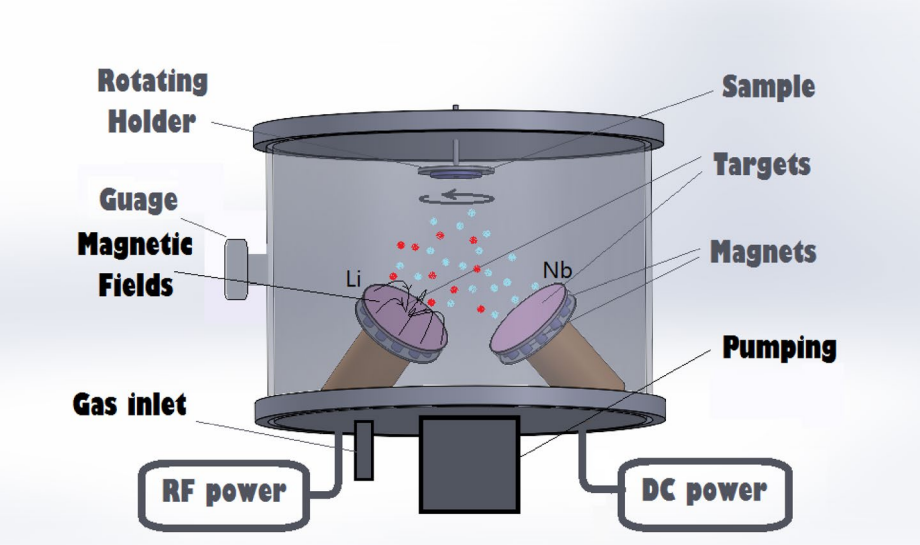


Fig. 1. Schematic diagram of the magnetron co-sputtering system.

water for 15 min to ensure removal of surface contaminants, then mounted in a rotating holder at a speed of 8 rpm. The substrate-to-target distance was fixed at 15 cm. To ensure high-vacuum conditions, the chamber pressure was reduced to 4.5×10^{-5} mbar using rotary and turbo molecular pumps. In the next step, 25 sccm of argon and 5 sccm of oxygen gases were introduced into the chamber. Mass flow controllers were used to adjust the gas flow ratio. A stepper motor-controlled Highvac valve was employed to maintain working pressure at 6×10^{-3} mbar. Before deposition, the targets were pre-sputtered in Ar plasma for 20 min. Different DC powers ranging from 20 to 80 W were applied to the niobium (Nb) target, while the lithium (Li) target was maintained at a constant RF power of 100 W. The Nb content in the films was controlled by adjusting the DC power. To achieve a gradual variation in Nb concentration, the DC power was increased in 10 W increments from 20 to 50 W. Additionally, a higher DC power of 80 W was applied to investigate the effects of elevated Nb input on film composition.

The reactive co-sputtering parameters are summarized in Table 1. Lithium (Li) metal targets are highly reactive and readily oxidize upon exposure to air. To prevent degradation, the Li target was supplied sealed in paraffin oil. Prior to initial use, it was thoroughly cleaned with acetone and immediately installed into the sputtering chamber. Under high-vacuum storage conditions, the target exhibited excellent resistance to oxidation and contamination. The deposition rate and film thickness were measured using a quartz crystal microbalance (QCM). To prevent moisture absorption, the prepared samples were stored in a desiccator and characterized without delay using a comprehensive set of analytical techniques.

Thin fim characterization

The crystal structure of the thin films was investigated using X-ray diffraction (XRD; Siemens D500) with Cu Kα radiation, scanning across a 2θ range of 20°–60° with a step size of 0.02°. Field emission scanning electron microscopy (FESEM; Tescan-Mira III) was used to examine the surface morphology of the films. To eliminate any charge effect, the samples were gold-sputtered. Energy-dispersive X-ray spectroscopy (EDX; Tescan Mira III), coupled with the FESEM system, was used to determine elemental distribution and chemical composition. X-ray photoelectron spectroscopy (XPS; Thermo K-Alpha) was used to characterize the surface chemistry of thin films, providing detailed information on the binding energies and chemical oxidation states of the constituent elements.

The Li-ion conductivity and dielectric properties of the films were evaluated using impedance spectroscopy on blocking-electrode cells configured in an Al/Li–Nb–O/Cu structure. Cross-plane Al/Li–Nb–O/Cu devices were fabricated by sequential sputtering through stainless steel shadow masks, which were manually exchanged between deposition steps to define the multilayer architecture. Fabrication commenced with the deposition of a 150 nm-thick aluminum (Al) film as the bottom electrode via DC sputtering of an Al target at 190 W. Them, a 200 nm Li–Nb–O film was deposited via co-sputtering through a separate mask. Circular top electrodes were fabricated by depositing a 150 nm-thick copper (Cu) film via DC sputtering of a Cu target at 100 W. Figure 2 schematically depicts the fabrication steps. This structure serves as a metal–insulator-metal (MIM) capacitor. The active electrolyte area between the electrodes was 19.63 mm^2. Electrical contact was established by attaching Au wires to the electrodes using silver adhesive paste. The impedance spectroscopy test were conducted using a KC-605 LCR meter, operating within a frequency range of 44 Hz to 100 kHz with an AC voltage amplitude of 10 mV. Temperature-dependent measurements were performed from room temperature to 110 °C, with 20 min equilibration at each step to ensure thermal stability.

Impedance spectra were analyzed by fitting the data using ZView electrochemical impedance spectroscopy (EIS) software (Version 3; available at [(https://www.scribner.com/software/68-general-electrochemistr376-zview-for-windows/)]). The Al/Li–Nb–O/Cu cells exhibited stable electrochemical performance, with no signs of lithium dendrite formation, instability, non-ideal behavior, or short-circuiting under low electric fields.

Results and discussion

Crystal structure analysis

The structural properties, including the crystallinity of the thin films, were examined using X-ray diffraction (XRD) analysis. No distinct peaks were observed in the XRD patterns of the Li–Nb–O films (Fig. 3), confirming their amorphous structure. This observation is consistent with the expected amorphous nature of sputter-deposited thin films at room temperature, as reported in literature[49]. During sputtering at low power, or without substrate heating or biasing, the low-energy particle impacts promotes growth along low-energy planes, yielding films with poor crystallinity. Recently, Rahn et al. reported that sputtered $LiNbO_3$ thin films remained amorphous after annealing up to 350 °C and started to crystallize only at 500 °C[50]. In this study, crystalline structure formation was achieved either by depositing thin films with substrate heating or through post-annealing; however, both methods resulted in lithium loss. Consequently, room-temperature deposition was chosen as the preferred

Sample	DC power (W)	RF power (W)	Base pressure (mbar)	Gass flow (Ar/O_2, sccm)	Working pressure (mbar)
1	20	100	4.5×10^{-5}	25/5	6×10^{-3}
2	30	100	4.5×10^{-5}	25/5	6×10^{-3}
3	40	100	4.5×10^{-5}	25/5	6×10^{-3}
4	50	100	4.5×10^{-5}	25/5	6×10^{-3}
5	80	100	4.5×10^{-5}	25/5	6×10^{-3}

Table 1. Co-sputtering parameters for the deposition of Li–Nb–O thin films.

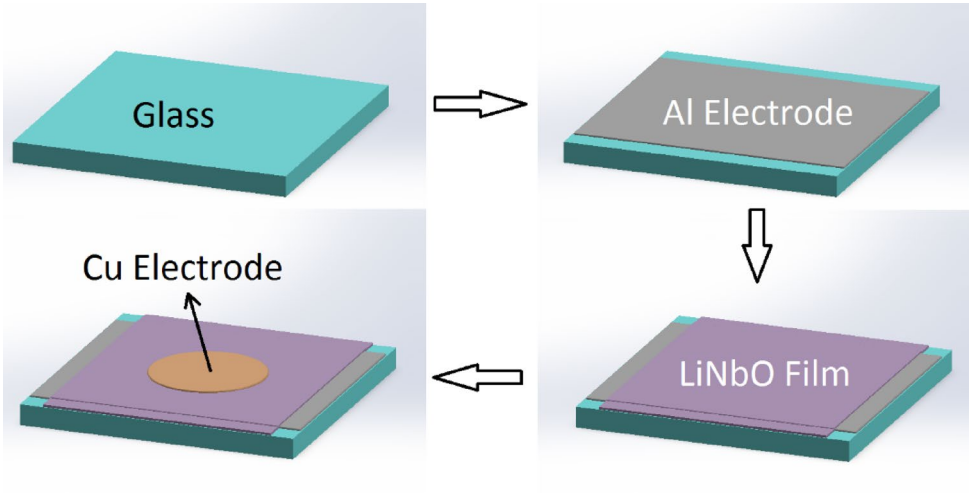


Fig. 2. Schematic illustration of cell fabrication processes.

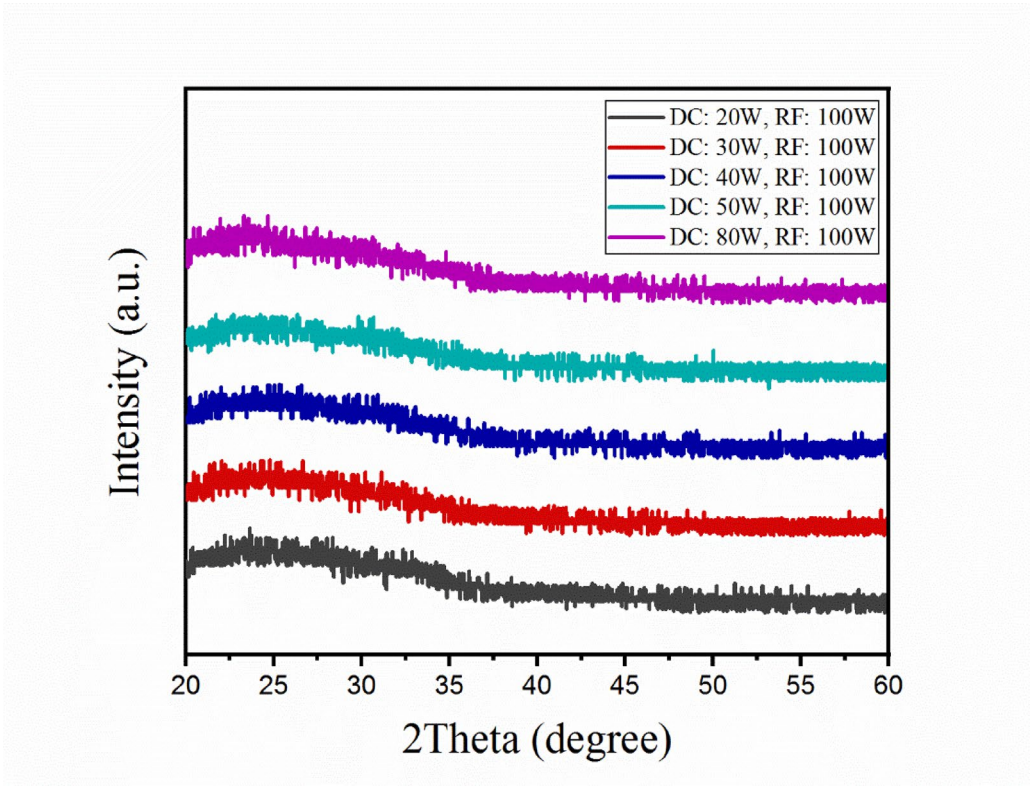


Fig. 3. XRD patterns of the as-deposited Li–Nb–O thin films.

approach. Previous studies have reported that single-crystal $LiNbO_3$ exhibits low ionic conductivity (~ 10^{-12} S cm^{-1} at 500 K), which limits its suitability as a solid-state electrolyte in LIBs[51]. Amorphous $LiNbO_3$ thin films are anticipated to exhibit higher ionic conductivity, primarily due to their inherent structural disorder and the absence of grain boundaries, which commonly impede ion transport in the crystalline lattice[52]. Moreover, amorphous thin-film electrolytes provide excellent surface compatibility with electrodes, effectively reducing interfacial resistance. This reduction is crucial for mitigating short-circuit risks and enhancing safety of Li-ion batteries and capacitors[23]. It is emphasized that amorphous layers are of great importance in various scientific and technological fields. They are preferred for application in transparent electronics, thin-film transistors, solar cells, memory devices, gravitational-wave detectors, and corrosion-resistant coatings[53,54].

Morphological characterization

Figure 4 presents FESEM images of the Li–Nb–O thin films. The surface morphology reveals a granular structure with the fine grains. Grain growth is evidently enhanced with increasing DC power, primarily due to two factors. First, higher DC power results in a greater number of target atoms being sputtered by Ar ion bombardment. Sputtered atoms with adequate kinetic energy can diffuse to favorable sites, facilitating effective atomic bonding

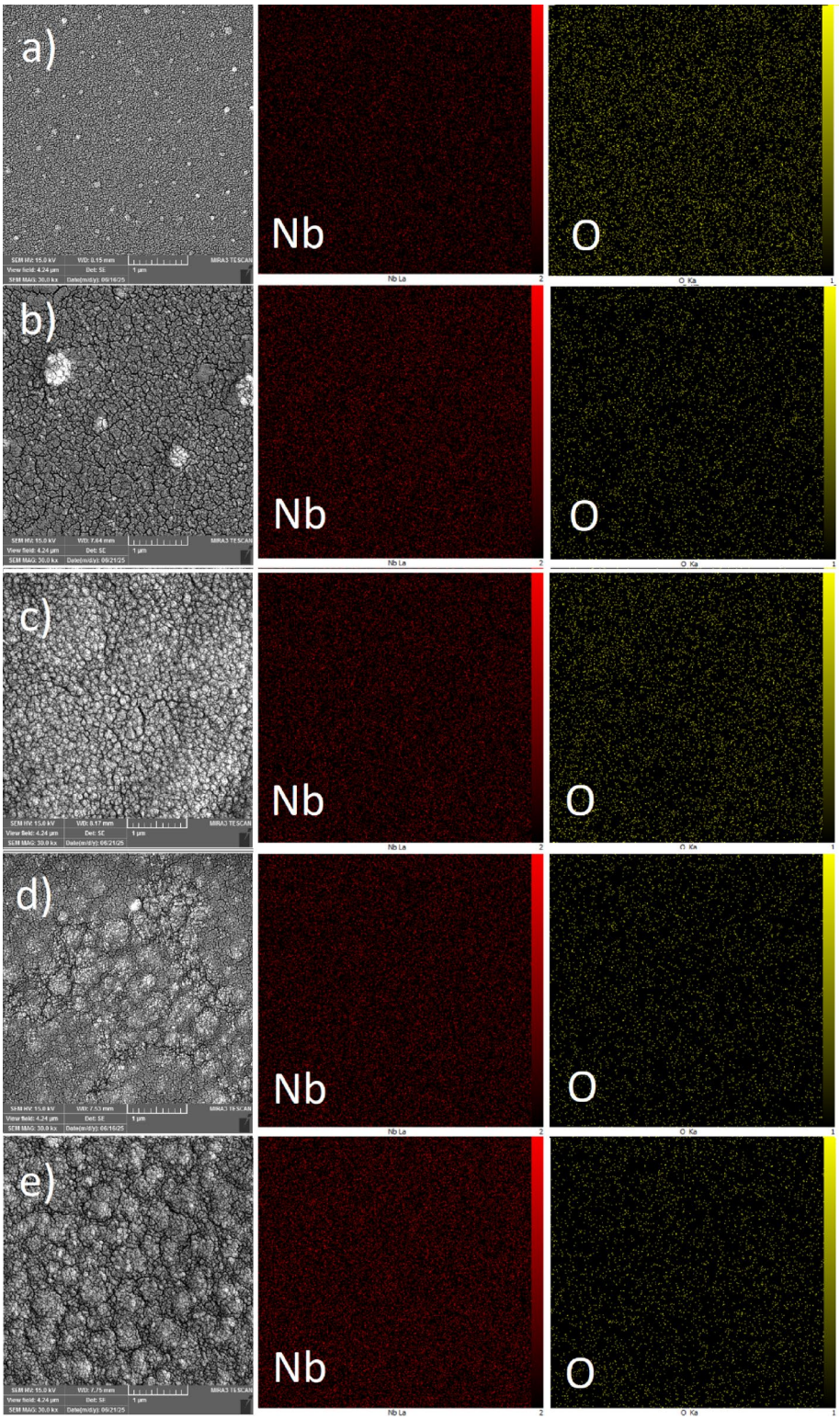


Fig. 4. FESEM images and corresponding EDX elemental maps of Nb and O for Li–Nb–O films deposited at constant RF power and various DC powers: (**a**) 20 W, (**b**) 30 W, (**c**) 40 W, (**d**) 50 W, and (**e**) 80 W.

and promoting grain growth. Secondly, the increase in substrate temperature due to high-energy bombardment promotes grain growth with well-defined boundaries[55].

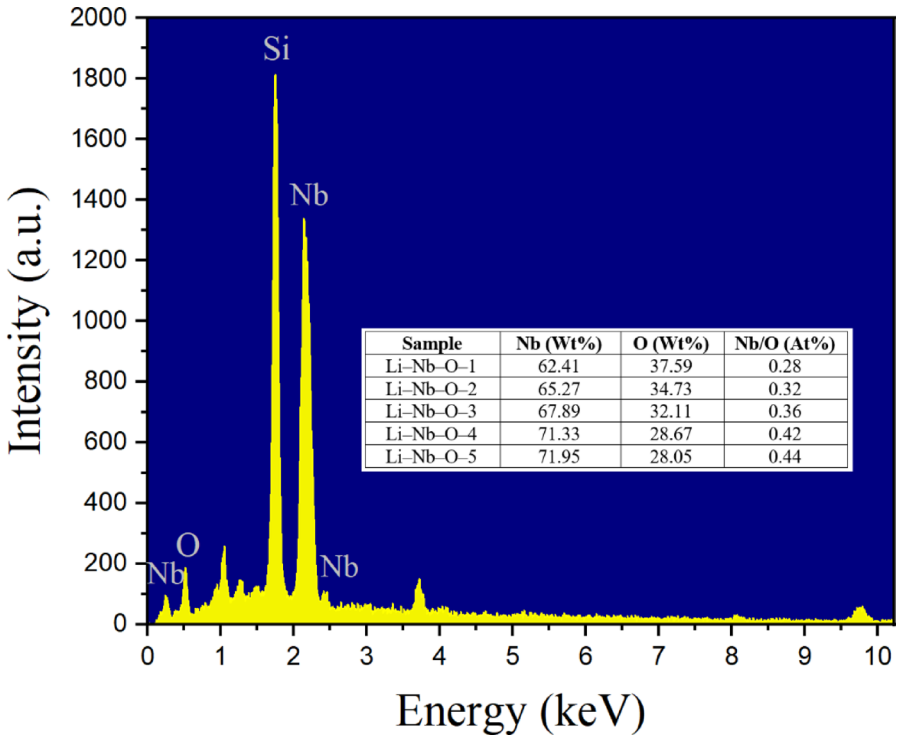
Energy-dispersive X-ray (EDX) spectroscopy was conducted to analyze the elemental distribution and chemical composition of the Li–Nb–O thin films. The EDX detector cannot identify Li due to the inherently low intensity of its Kα X-ray emission line. As shown in Fig. 4, the EDX mapping results demonstrate a homogeneous distribution of the constituent elements, including niobium (Nb) and oxygen (O), across the films. This result indicates the absence of significant Nb agglomeration on surface, thereby promoting uniform material formation. Such uniformity is an essential criterion for consistent electrochemical performance and mechanical stability. Figure 5 displays the selected EDX spectrum for the Li–Nb–O sample deposited at a DC poswer of 80 W. Si peak is attributed to the glass substrate. The Nb-to-O atomic ratio was determined from the EDX measurements, yielding values in the range of 0.28–0.44, as presented in the inset table of Fig. 5. A systematic increase in the Nb/O ratio with increasing DC sputtering power was observed, reflecting the progressive increase in Nb content.

Chemical composition analysis

XPS analysis was used to characterize the elemental composition and oxidation states of the constituent species in Li–Nb–O films deposited at various DC powers. Figure 6a displays the XPS survey scan spectra of the films, confirming the presence of Li, Nb, O, and C, in agreement with previously reported results[56]. No impurities were detected except carbon, attributed to surface contamination; the C 1s peak at 284.5 eV was used as an internal standard to calibrate all XPS spectra for charge compensation. XPS is a surface-sensitive method that quantifies elemental composition in the near-surface region of a sample. The lithium content, as one of the most critical parameters affecting ionic conductivity, was experimentally evaluated by XPS analysis. However, due to the weak Nb signal in XPS spectra, the Nb atomic ratio was further determined using EDX analysis. The combined application of EDX and XPS enabled a quantitative assessment of the film composition.

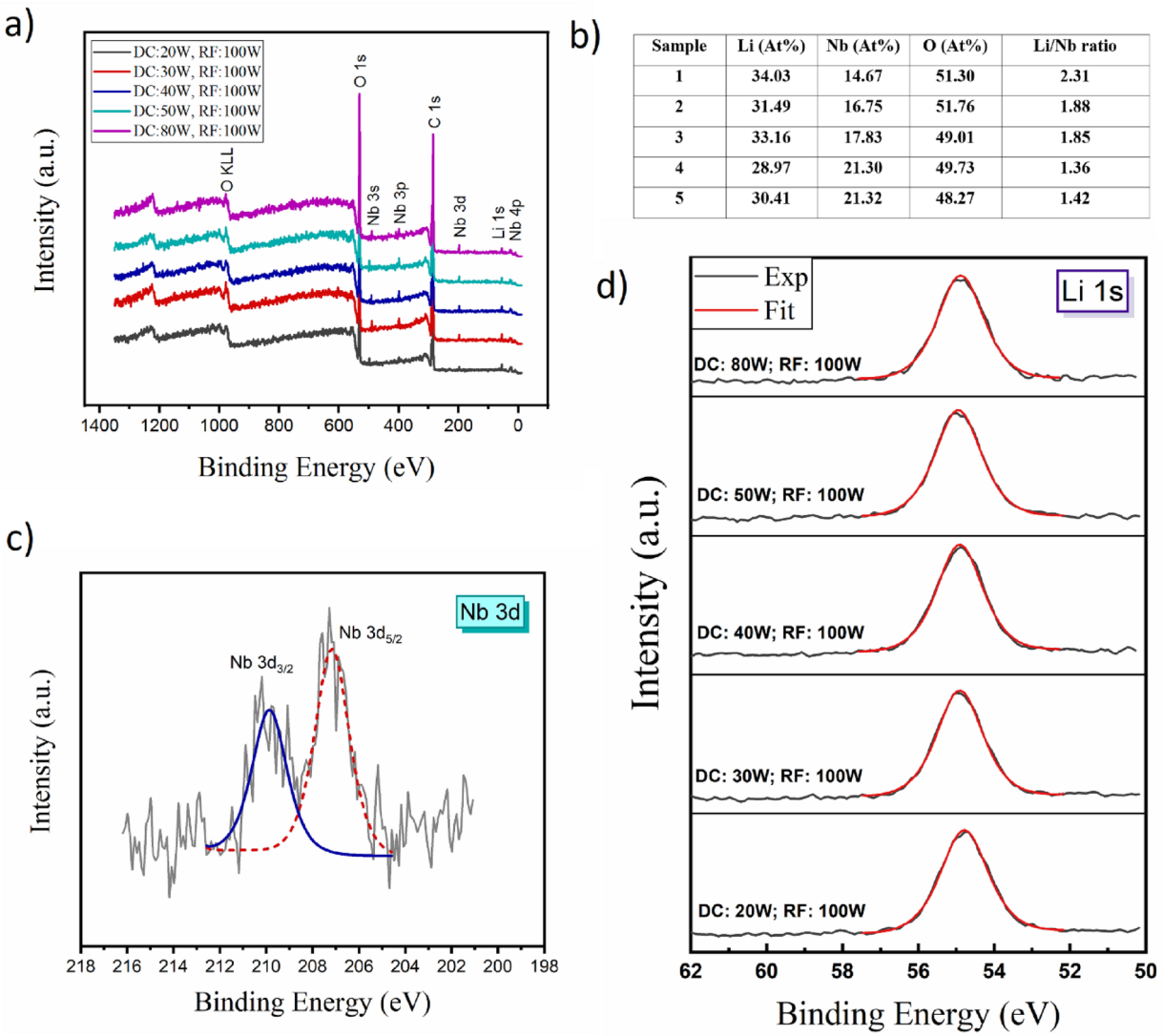
The atomic percentages of the constituent elements are summarized in the table presented in Fig. 6b. Examination of the relative Li and Nb content in the film surface reveals how maintaining a relatively high constant RF power on the Li target, while varying DC power applied to Nb target, affects the chemical composition. To clarity regarding the compositional region of the Li–Nb–O ternary system, the Li-to-Nb content ratio was calculated, yielding values in the range of 2.31–1.36. This indicates the successful achievement of a Li-rich compositional region. As shown in Fig. 6b, the Li/Nb atomic ratio exhibits a general decreasing trend with increasing DC power. This result is in agreement with the corresponding enhancement in Nb content.

Figure 6c presents the high-resolution Nb 3d core-level spectrum of the Li–Nb–O film deposited at a DC power of 80 W. This sample was selected for detailed study because films deposited at lower DC powers contain reduced niobium content, resulting in significantly weaker Nb 3d signal intensity. The spectrum exhibits a Nb $3d_{3/2}$–Nb $3d_{3/2}$ doublet, with peak centers located at binding energies of 209.87 eV and 207.16 eV, respectively. These values with the spin–orbit splitting of approximately 2.7 eV are characteristic of Nb^{5+} oxidation state and



Sample	Nb (Wt%)	O (Wt%)	Nb/O (At%)
Li–Nb–O–1	62.41	37.59	0.28
Li–Nb–O–2	65.27	34.73	0.32
Li–Nb–O–3	67.89	32.11	0.36
Li–Nb–O–4	71.33	28.67	0.42
Li–Nb–O–5	71.95	28.05	0.44

Fig. 5. EDX spectrum of the Li–Nb–O sample deposited at a DC power of 80 W, along with the EDX analysis table summarizing all samples.



Sample	Li (At%)	Nb (At%)	O (At%)	Li/Nb ratio
1	34.03	14.67	51.30	2.31
2	31.49	16.75	51.76	1.88
3	33.16	17.83	49.01	1.85
4	28.97	21.30	49.73	1.36
5	30.41	21.32	48.27	1.42

Fig. 6. (**a**) XPS survey spectra of Li–Nb–O films, (**b**) XPS analysis table summarizing all samples, (**c**) Nb 3d core-level spectrum, and (**d**) Li 1s core-level spectra.

align well with values reported in the literature[57]. In this study, the Nb 4s peak was not observed in the XPS spectra. This is due to the Li/Nb ratio exceeding 1.0, confirming the formation of a Li-rich phase.

Figure 6d displays the Li 1s core-level spectra of the films, each characterized by a single sharp and symmetric peak centered at ~ 54.78 eV. This indicates the monovalent chemical state of Li^+ ions in all samples[23]. The comparable intensities of the Li 1s XPS peaks observed across the films can be ascribed to the application of constant RF power to the Li target during sputtering.

Figure 7 presents the O 1s core-level spectra of th Li–Nb–O thin films. The O 1s peaks were deconvoluted to 530.61, 531.45, and 532.67 eV, corresponding to Nb-oxygen, Li–O, and Li–OH bonds, respectively[56,58]. The presence of hydroxyl species is attributed to the absorption of moisture during exposure to the ambient atmosphere. Figure 7f depicts the variation in relative quantities of Nb–O and Li–O bonds as a function of DC sputtering power. The integrated area of the 530.61 eV peak gradually increased (3.19–11.51%) with rising DC power (20–80 W), indicating enhanced Nb–O bond formation. This enhancement is attributed to the higher Nb concentration achieved at increased sputtering power. In contrast, the fraction of O^{2-} associated with Li–O bonds decreased from 79.81 to 70.52% over the same DC power range. This result suggests a greater contribution from weakly bonded Li^+ ions, which predominantly govern ionic conductivity in disordered solids.

Impedance spectroscopy

Impedance spectroscopy was conducted on the Al/Li–Nb–O/Cu configuration to evaluate the effect of co-sputtering parameters on carrier transport and charge storage. The schematic and cross-sectional FESEM image of this structure are shown in Fig. 8a, b, respectively. The contacts act as blocking electrodes for Li ions under an

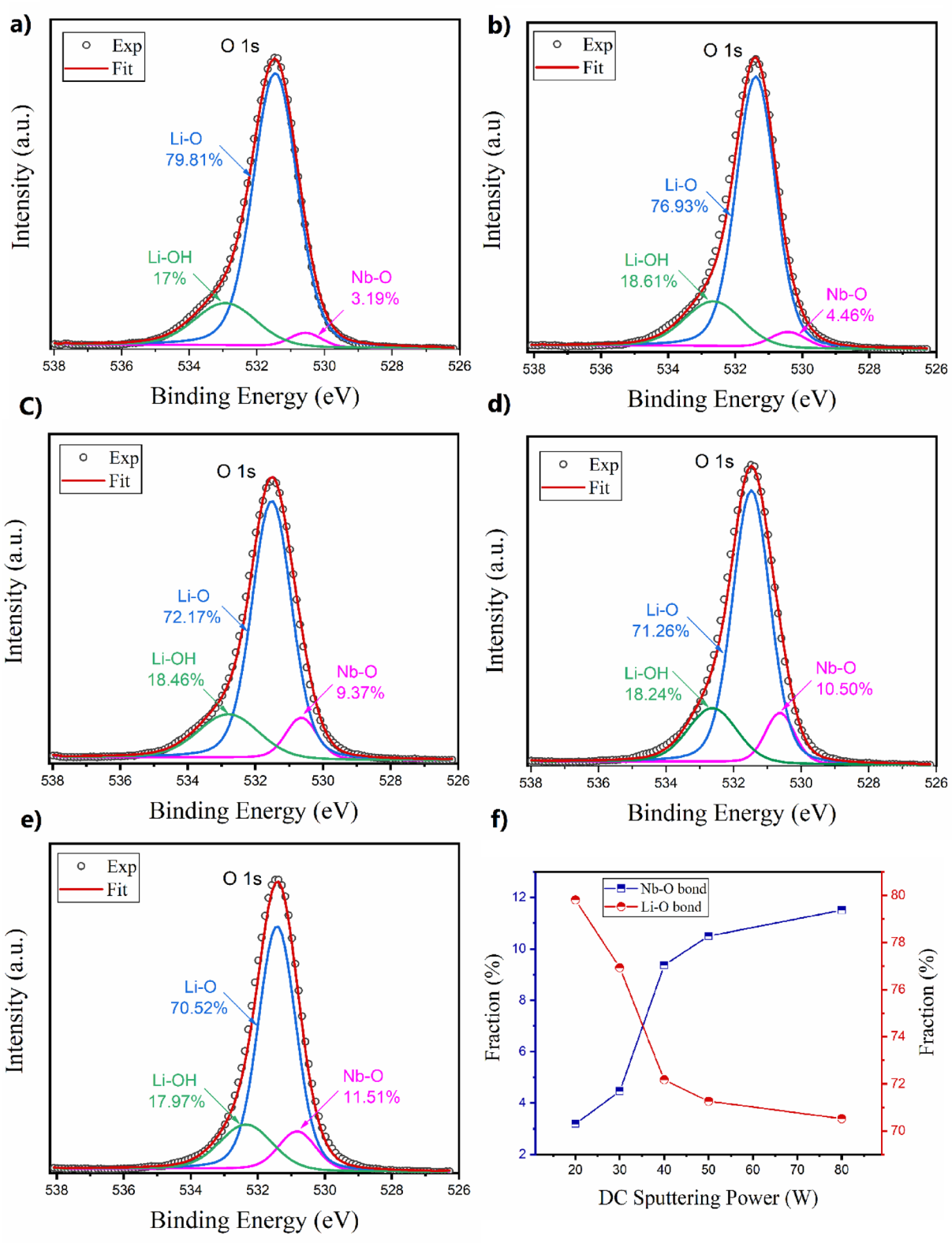


Fig. 7. O1s core-level spectra of the Li–Nb–O films deposited at a DC power of (**a**) 20 W, (**b**) 30 W, (**c**) 40 W, (**d**) 50 W, (**e**) 80 W; and (**f**) the relative intensity of oxygen bonds as a function of DC sputtering power.

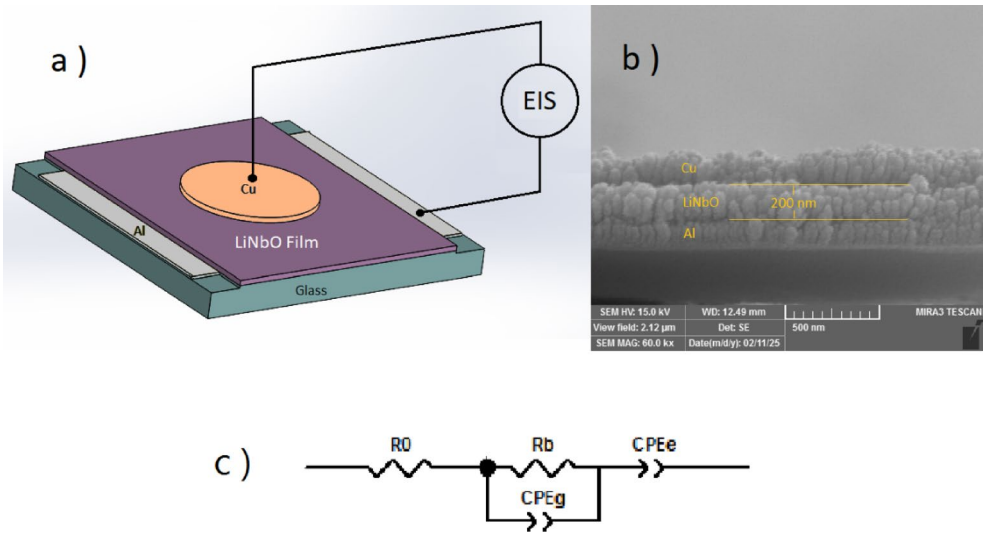


Fig. 8. (**a**) Schematic diagram, (**b**) cross-sectional FESEM image, and (**c**) equivalent circuit model of the Al/LiNbO/Cu structure.

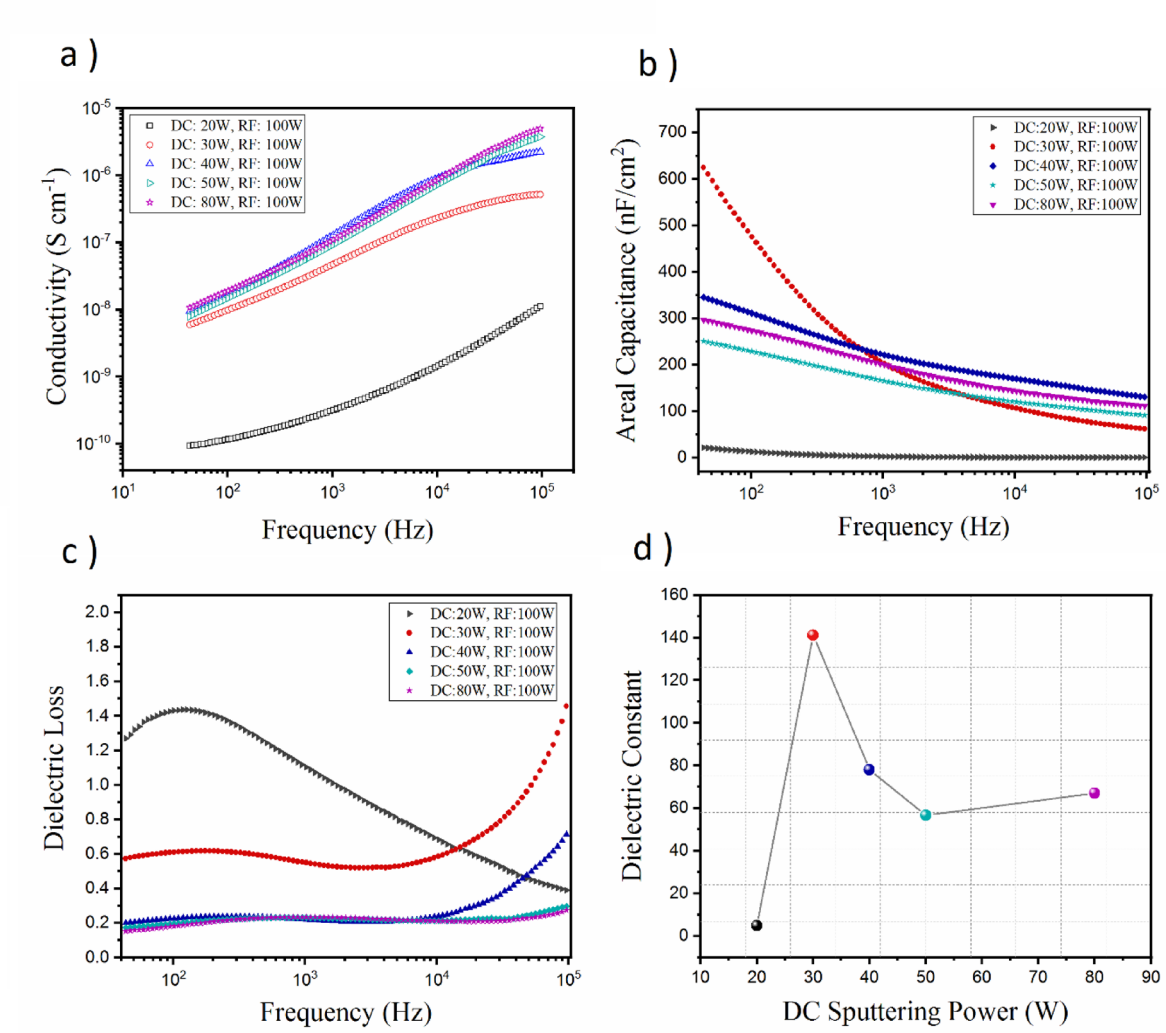


Fig. 9. Frequency dependence of (**a**) a.c. conductivity, (**b**) areal capacitance, and (**c**) dielectric loss for Li–Nb–O films. (**d**) Dielectric constant as a function of DC sputtering power.

alternating electric field. The impedance response depends primarily on material type, synthesis method, and measurement temperature. Other factors, such as crystal structure, chemical composition, and grain boundary distribution, also influence the overall impedance behavior.

Frequency dependence of a.c. conductivity and dielectric properties

Figure 9a presents the a.c. conductivity of Li–Nb–O thin films measured at room temperature. Electrical conductivity in solid-state electrolytes is a thermally-activated process, governed by the migration of weakly bound ions under an applied electric field[59]. Frequency dependence of σ(ω) for all Li–Nb–O films follows Jonscher's power law[60]:

$$\sigma(\omega) = \sigma_{dc} + A\omega^{n},\ 0 \le n \le 1 \tag{1}$$

Here, σ_{dc} is the dc conductivity, A is a pre-exponential factor related to polarizability, ω is the angular frequency, and n is an experimentally determined fitting parameter. The parameter n reflects the interaction degree between charge carriers and surrounding lattice. The exponent "n" is frequency-independent but can vary with the type of mobile ion, ion concentration, and system temperature. The universal dynamic response (UDR) in disordered solids is described by Jonscher's law.

A significant increase in σ(ω) was observed as the DC sputtering power increased from 20 to 30 W, followed by a slight increase between 40 and 80 W. Ionic transport primarily depends on factors such as ionic polarizability, Li–O binding strength, Li ion contribution, hydration radius, and vacancy density. Additionally, Li^{+}–Li^{+} Coulombic interactions and ion-electrode interactions play critical roles in overall transport behavior[61]. Here, enhanced ionic conductivity is directly correlated with the increased number of sputtered Nb atoms due to higher DC sputtering power.

With increasing Nb concentration, Nb atoms exhibit a strong tendency to occupy Li sites. This behavior is primarily attributed to the similar ionic radii of Nb (0.64 Å) and Li (0.76 Å), as well as the difference in bond strengths within the Li–Nb–O system. The Nb–O covalent bond (E_b ~ 567.31 kJ/mol) is considerably

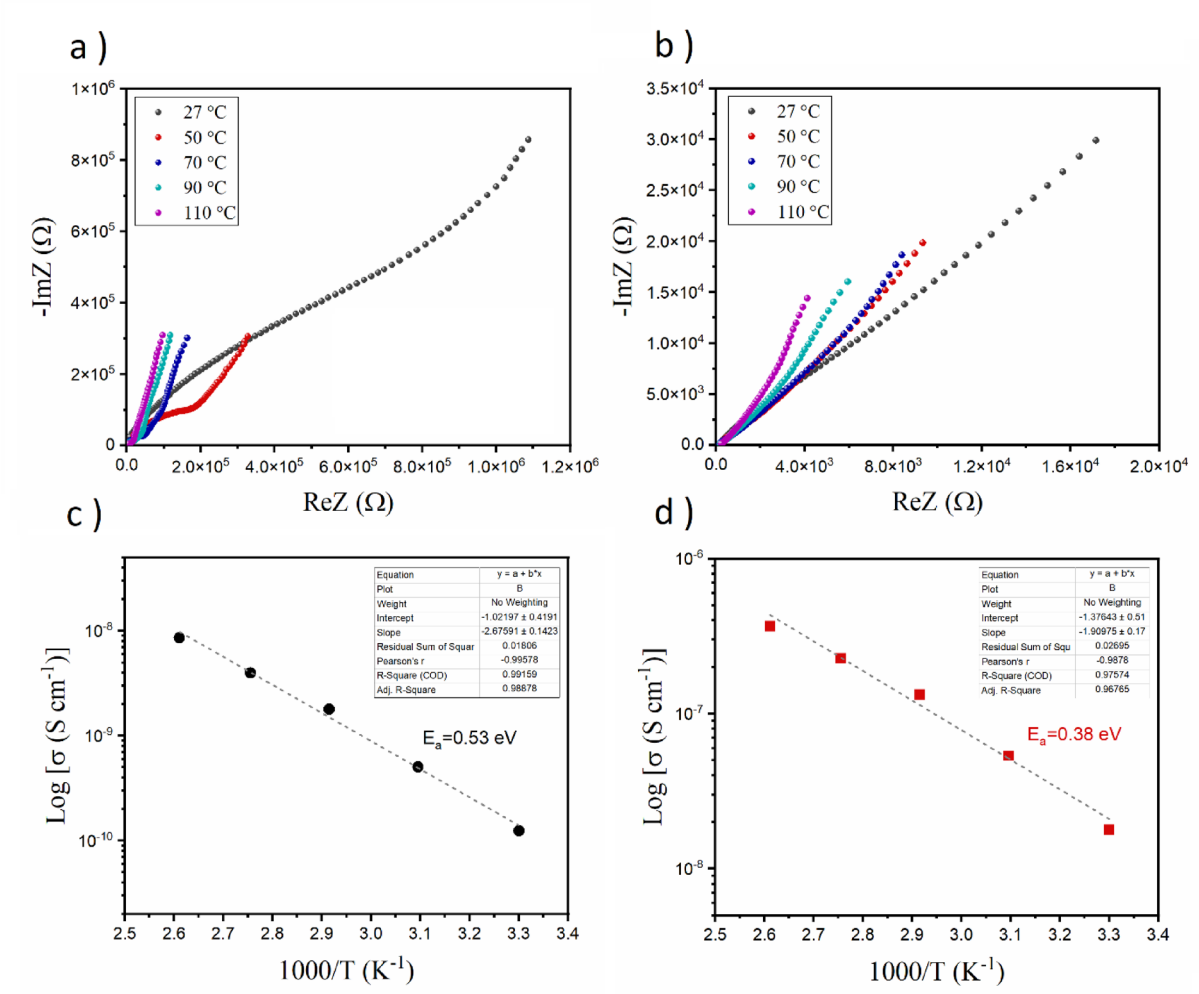


Fig. 10. Nyquist plots of co-sputtered films at DC power of (**a**) 20 W, and (**b**) 30 W. Arrhenius plots of the corresponding films at DC powers of (**c**) 20 W and (**d**) 30 W.

Sample	σ_{dc} (S cm^{-1})	Ci (nF cm^{-2})	K	Loss at 100 Hz
1	1.25×10^{-10}	21.80	4.92	1.43
2	1.78×10^{-8}	624.86	141.21	0.61
3	4.16×10^{-8}	345.45	78.06	0.22
4	8.04×10^{-8}	250.73	56.66	0.19
5	1.33×10^{-7}	297.10	67.14	0.18

Table 2. Ionic conductivity, areal capacitance, dielectric constant, and dielectric loss for the co-sputtered Li–Nb–O films.

Materials	σ_{RT} (S cm^{-1})	Synthesis techniques	Refs.
Li–Nb–O films	1.33×10^{-7}	Magnetron co-sputtering	This work
Li–Nb–O films	6.39×10^{-8}	Atomic layer deposition	[34]
$LiNbO_3$ films	2×10^{-8}	RF sputtering	[74]
$LiNbO_3$ nanocrystalline	7.20×10^{-6}	aqueous solution	[77]
$LiNbO_3$ films	$6–8\times10^{-7}$	Sol–gel	[78]

Table 3. Overview of room-temperature ionic conductivity values of Li–Nb–O reported in recent studies.

stronger than the Li–O ionic bond ($E_b \sim 392.50$ kJ/mol), favoring Nb substitution at Li sites and the formation of Li vacancies[62]. Substitution of monovalent Li^+ by pentavalent Nb^{5+} disrupts charge neutrality, promoting the formation of additional Li^+ vacancies. These vacancies serve as diffusion sites, facilitating Li-ion transport within the Li–Nb–O framework. Moreover, the presence of Li^+ vacancies reduces Li^+–Li^+ electrostatic repulsion, thereby further enhancing ionic mobility[63]. XPS analysis confirms predominant Nb–O bond formation and a reduction in the concentration of bonded Li ions with increasing DC power.

Measuring dc conductivity of electrolyte films is challenging due to the ionic polarization at low frequencies and bulk ionic transport at high frequencies. The σ_{dc} value can approximated as $\sigma(\omega)$ at the frequency of peak in loss spectrum. This approximation agrees well with the results obtaine from fitting Nyquist plots (Z''–Z') using an equivalent circuit model[64]. The room-temperature σ_{dc} values for the co-sputtered Li–Nb–O thin films are listed in Table 2. The maximum σ_{RT} value obtained was 1.33×10^{-7} S cm^{-1}, comparable to previously reported results for $LiNbO_3$ (Table 3). This value is even higher than that reported for material synthesized by other methods. For example, Wang et al. recently reported a σ_{RT} of 6.39×10^{-8} S cm^{-1} for Li–Nb–O thin films grown by ALD at a deposition temperature of 235 °C[34]. This indicates the potential of co-sputtering to produce thin-film electrolytes with improved ionic conductivity. In this study, Li–Nb–O films provide moderate σ_{RT} value, surpassing comparable amorphous systems such as Li–Ta–O ($\sigma_{RT} \sim 10^{-8}$ S cm^{-1}) and Li–Al–O ($\sigma_{RT} \sim 2.85\times10^{-9}$ S cm^{-1})[21,65].

Figure 9b shows the capacitance-frequency curves of Li–Nb–O based MIM capacitors at room temperature. The low-frequency capacitance of the samples is presented in Table 2. The highest C_i value (625 nF cm^{-2}) was achieved for film prepared at a DC power of 30 W. This behavior is directly related to the ionic conduction mechanism. Incorporation of Li ions into niobium oxide induces a complex process that enhances charge storage, associated with the electrode polarization effect. This is attributed to the formation of electric double layers (EDLs), resulting from the ion accumulation at the blocking electrolyte/electrode interfaces.

In the low-frequency range, Li^+ ions are able to respond to external electric field and undergo long-range diffusion, leading to resistive behavior. With increasing frequency, sharp decline in capacitance is attributed to reduced effective ionic polarization. This behavior is due to the inability of Li^+ ions to follow the rapidly oscillating electric field. At high frequencies, the plateau observed in C_i suggests that induced dipoles fail to respond to the electric field. This is related to the limited time available for dipolar rotation or ionic displacement[66].

The dielectric constant (k) of a metal–insulator-metal (MIM) capacitor can be calculated using the following formula:

$$C_i = \frac{k\varepsilon_0}{d} \tag{2}$$

Here, C_i represents the capacitance per unit area, ε_o is the vacuum permittivity, and d is the thickness of the dielectric layer. The obtained k values for the Li–Nb–O thin films are shown in Fig. 9d. These results indicate that all layers can be classified as ion-conducting dielectric. The maximum dielectric constant (k) was measured to be 141.21, significantly exceeding the values reported for materials synthesized via alternative methods, as summarized in Table 4. Notably, the Li–Nb–O thin films exhibit a higher dielectric constant compared to pure Nb_2O_3 ($k \sim 47$), confirming the contribution of the electric double layer (EDL) effect[67]. Similarly, Nila Pal et al. reported an increase in dielectric constant of Al_2O_3 from 8.8 to 35 upon the incorporation of Li ions into the film using a sol–gel process[68].

Dielectric loss, the ratio of dissipated to stored energy, can be calculated in terms of the real (ε') and imaginary (ε'') components of the permittivity as follows[65]:

Materials	K	Synthesis techniques	Refs.
Li–Nb–O films	141.21	Magnetron co-sputtering	This work
$LiNbO_3$ films	8.01	Thermal evaporation	[33]
$LiNbO_3$ films	35	Sol–gel	[79]
$LiNbO_3$ films	38.20	RF magnetron sputtering	[80]

Table 4. Comparison of dielectric constants for the Li–Nb–O system.

$$\tan\delta = \varepsilon''/\varepsilon' \tag{3}$$

Figure 9 c presents room-temperature loss tangent plots; corresponding values at 100 Hz are listed in Table 2. The Li–Nb–O thin films with low ionic conductivity exhibit a pronounced relaxation peak. In contrast, higher ionic conductivity leads to a suppression of this feature, yielding a nearly flat loss profile with minimal dielectric loss value.

The loss peak delineates the low- and high-frequency regimes, reflecting resonance between the applied electric field and the characteristic dipolar relaxation frequency. At the resonant condition ($\omega\tau = 1$), power transfer from the external source to the dipolar system is maximized. This results in peak energy dissipation and the corresponding thermal response[69]. The absence of a loss peak arises from dominance of electrode polarization over dipolar relaxation, known as the masking effect. The observed decrease in the dielectric loss is attributed to the enhanced Li^+ ion mobility. The accelerated response of Li–Li dipoles under applied alternating field leads to a reduced relaxation time. Sharma et al. reported that a zero relaxation time leads to the dielectric loss approaching zero ($\varepsilon'' = 0$ for $\omega\tau = 0$) [70].

Temperature dependence of a.c. conductivity and dielectric properties

To investigate the thermally-activated diffusion of lithium ions, impedance spectroscopy was performed over the temperature range of 27–110 °C. Figure 10a, b display the Nyquist plots of Li–Nb–O films deposited at DC powers of 20 W and 30 W, respectively. To extract accurate information from the impedance diagrams, modeling and fitting of Nyquist plots were carried out using ZView software. The corresponding equivalent circuit used to model the system is shown in Fig. 8c. In this circuit, R_0 represents the ohmic resistance of the electrical contacts. Typically, Nyquist plots exhibit a semicircle in the high-frequency region and an inclined line at low frequencies. The high-frequency semicircular arc reflects the bulk response of the films and is modeled by a bulk resistance (R_b) in parallel with a constant phase element (CPE_g). At low frequencies, the inclined line is attributed to dominant ionic conduction. This feature is represented in the equivalent circuit by a constant phase element (CPE_e), which captures stray capacitive behavior arising from ion accumulation at the electrode/electrolyte interface.

The ionic conductivity (σ) of Li–Nb–O films at various temperatures can be calculated from the fitted bulk resistance (R_b) using the following equation[71]:

$$\sigma = L/(R_b \times S) \tag{4}$$

Here, L denotes the film thickness, corresponding to the length of conduction pathway, and S represents the contact area between the electrolyte and the electrodes. As shown in Fig. 10c, d, the exponential increase in ionic conductivity with rising temperature follows the Arrhenius relation[72]:

$$\sigma_T = \sigma_0 \exp\left(E_a/k_B T\right) \tag{5}$$

Here, σ_T denotes the ionic conductivity, σ_0 is the pre-exponential factor, E_a represents the activation energy, k_B is the Boltzmann constant, and T is absolute temperature. The activation energy (E_a) can be extracted from the linear fit of $\log(\sigma_T)$ versus 1/T. The Li–Nb–O films deposited at a DC power of 20 W exhibits an activation energy of 0.53 eV, which is comparable to reported values ranging from 0.4 to 0.65 eV for lithium niobate in previous studies[34,73–76]. For films deposited at a DC power of 30 W, the activation energy was determined to be 0.38 eV. The observed decrease in E_a with increasing DC power is attributed to the substitution of Li^+ ions by Nb^{5+}, leading to an increased concentration of Li^+ vacancies. These vacancies facilitate the lower-energy transport of Li^+ ions by creating favorable diffusion pathways and reducing Coulombic repulsion between adjacent Li^+ ions[63].

Figure 11a, b exhibit a noticeable enhancement in capacitance with rising temperature. This is attributed to improved electrode polarization caused by thermally-activated processes. The optimized Li–Nb–O based MIM capacitors (DC: 30 W; RF: 100 W) exhibited a maximum low-frequency capacitance of 1.3 μF cm^{-2}, corresponding to a dielectric constant of 293 at 110 °C.

Figure 11c, d shows the loss spectra of the Li–Nb–O films at various temperatures. As the temperature increases, the relaxation peak shifts to higher frequencies, concomitant with a reduction in peak intensity. This indicates a reduction in relaxation time due to enhanced ion diffusion[71].

Conclusion

In summary, this study examined the structural, morphological, and electrical properties of Li–Nb–O thin films synthesized via reactive co-sputtering, with varying DC powers applied to the Nb target and a constant RF power for the Li target. X-ray diffraction confirmed the amorphous nature of all samples. FESEM analysis

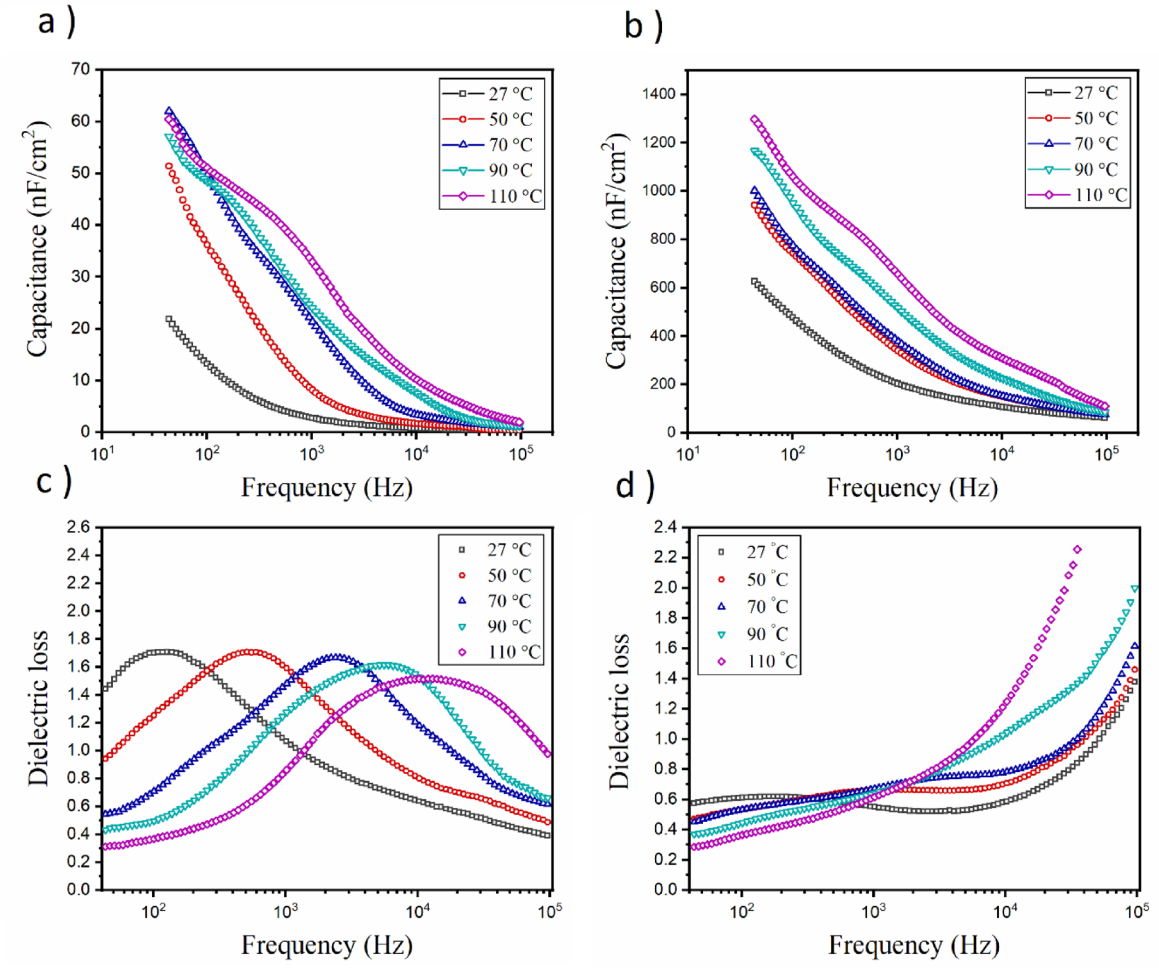


Fig. 11. Temperature dependence of capacitance for films deposited at DC powers of (**a**) 20 W and (**b**) 30 W. Temperature dependence of dielectric loss for the corresponding films at DC powers of (**c**) 20 W and (**d**) 30 W.

revealed that surface morphology was significantly affected by increasing DC power. EDX measurements showed a rise in Nb/O atomic ratio from 0.28 to 0.44 as the DC power increased (20–80 W). XPS studies confirmed the predominance of Nb–O bonding, along with an increased presence of weakly bound Li ions at higher Nb concentrations. Furthermore, the Li-to-Nb atomic ratio was found to vary between 2.31 and 1.36, consistent with the formation of a Li-rich region. Impedance spectroscopy demonstrated an enhancement in the ionic conductivity, reaching 1.33×10^{-7} S cm^{-1} at room temperature. Notably, the optimized Li-Nb–O capacitor exhibited a high areal capacitance (~ 624.86 nF cm^{-2}), a maximum dielectric constant (~ 141.21), and a low loss. These results highlight co-sputtering as an effective route for developing Li–Nb–O thin films tailored for next-generation solid-state energy storage devices.

Data availability

The datasets used and/or analysed during the current study available from the corresponding author on reasonable request.

Received: 31 July 2025; Accepted: 23 September 2025
Published online: 29 October 2025

References

1. Zhang, P., Wang, F., Yu, M., Zhuang, X. & Feng, X. Two-dimensional materials for miniaturized energy storage devices: From individual devices to smart integrated systems. *Chem. Soc. Rev.* **47**, 7426–7451 (2018).
2. Wang, Z. et al. Miniaturized lithium-ion batteries for on-chip energy storage. *Nanoscale Adv.* **4**, 4237–4257 (2022).
3. Wu, B., Chen, C., Danilov, D. L., Eichel, R.-A. & Notten, P. H. All-solid-state thin film li-ion batteries: New challenges, new materials, and new designs. *Batteries* **9**, 186 (2023).
4. Khan, H. A. et al. A comprehensive review on supercapacitors: Their promise to flexibility, high temperature, materials, design, and challenges. *Energy* **295**, 131043 (2024).

5. Yan, R. et al. Enhanced ionic conductivity and excellent lithium stability of garnet-type $Li_{6.55}Ga_{0.15}La_3Zr_2O_{12}$ solid-state electrolytes by magnesium doping. *J. Energy Storage* **87**, 111481 (2024).
6. Wang, Q., Jiang, L., Yu, Y. & Sun, J. Progress of enhancing the safety of lithium ion battery from the electrolyte aspect. *Nano Energy* **55**, 93–114 (2019).
7. Tapia-Ruiz, N. et al. Low dimensional nanostructures of fast ion conducting lithium nitride. *Nat. Commun.* **11**, 4492 (2020).
8. Jouybari, Y. H., Berkemeier, F., Schäfer, A. & Schmitz, G. The influence of sputter conditions on the properties of LiPON and its interfaces. *J. Power Sources* **394**, 160–169 (2018).
9. Bharathi, P. & Wang, S.-F. Nanoscale synthesis of $Li_{1.3}Al_{0.3}Ti_{1.7}(PO_4)_3$ solid-state lithium ion battery electrolyte: A structural and ionic conductivity study. *ACS Appl. Nano Mater.* **7**, 1615–1624 (2024).
10. Chouiekh, A. et al. Experimental and DFT analysis of structural, optical, and electrical properties of $Li_{3x}La_{2/3-x}TiO_3$ (3x = 0.1, 0.3 and 0.5) solid electrolyte. *Ceram. Int.* **49**, 25920–25934 (2023).
11. Yan, Z. & Zhu, Y. Impact of lithium nonstoichiometry on ionic diffusion in tetragonal garnet-type $Li_7La_3Zr_2O_{12}$. *Chem. Mater.* **36**, 11551–11557 (2024).
12. Hikima, K. et al. Electrochemical properties of $Li_{10}GeP_2S_{12}$ solid electrolytes synthesized using a solution-based method. *ACS Appl. Energy Mater.* **7**, 8788–8796 (2024).
13. Maltsev, A. P., Chepkasov, I. V. & Oganov, A. R. Order–disorder phase transition and ionic conductivity in a $Li_2B_{12}H_{12}$ solid electrolyte. *ACS Appl. Mater. Interfaces* **15**, 42511–42519 (2023).
14. Wang, C., Liang, J., Kim, J. T. & Sun, X. Prospects of halide-based all-solid-state batteries: From material design to practical application. *Sci. Adv.* **8**, eadc9516 (2022).
15. Janek, J. & Zeier, W. G. A solid future for battery development. *Nat. Energy* **1**, 1–4 (2016).
16. Zhu, Y. et al. Lithium-film ceramics for solid-state lithionic devices. *Nat. Rev. Mater.* **6**, 313–331 (2021).
17. Dudney, N. J. & Jang, Y.-I. Analysis of thin-film lithium batteries with cathodes of 50 nm to 4 μm thick $LiCoO_2$. *J. Power Sources* **119**, 300–304 (2003).
18. Tyagi, A., Tripathi, K. M. & Gupta, R. K. Recent progress in micro-scale energy storage devices and future aspects. *J. Mater. Chem. A* **3**, 22507–22541 (2015).
19. Ohnishi, T. & Takada, K. Sputter-deposited amorphous Li_3PO_4 solid electrolyte films. *ACS Omega* **7**, 21199–21206 (2022).
20. Jafarpour, S., Naghshara, H. & Aslibeiki, B. Structural, optical, and dielectric properties of ion-conducting $LiAlO_2$ thin films produced by reactive magnetron co-sputtering. *ACS Appl. Electron. Mater.* **5**, 1566–1574 (2023).
21. Hu, Y. et al. Ionic conductivity in LixTaOy thin films grown by atomic layer deposition. *Electrochim. Acta* **361**, 137019 (2020).
22. Mousavi, T. et al. Fabrication of $Li_{1+x}Al_xGe_{2-x}(PO_4)_3$ thin films by sputtering for solid electrolytes. *Solid State Ionics* **354**, 115397 (2020).
23. Tan, G., Wu, F., Li, L., Liu, Y. & Chen, R. Magnetron sputtering preparation of nitrogen-incorporated lithium–aluminum–titanium phosphate based thin film electrolytes for all-solid-state lithium ion batteries. *J. Phys. Chem. C* **116**, 3817–3826 (2012).
24. Mei, H.-X., Piccardo, P., Carraro, G., Smerieri, M. & Spotorno, R. Thin-film Li_3InCl_6 electrolyte prepared by solution casting method for all-solid-state batteries. *J. Energy Storage* **72**, 108244 (2023).
25. Hüger, E. et al. Lithium niobate for fast cycling in Li-ion batteries: Review and new experimental results. *Batteries* **9**, 244 (2023).
26. Pal, N. et al. Solution processed Li-Al_2O_3/$LiNbO_3$/Li-Al_2O_3 stacked gate dielectric for a non-volatile ferroelectric thin film transistor. *J. Alloys Compd.* **960**, 170691 (2023).
27. Atak, G. & Coşkun, Ö. D. $LiNbO_3$ thin films for all-solid-state electrochromic devices. *Opt. Mater.* **82**, 160–167 (2018).
28. Chen, X. et al. High performance lithium niobate surface acoustic wave transducers in the 4–12 GHz super high frequency range. *J. Vacuum Sci. Technol. B* **33**, 06F401 (2015).
29. Zhang, M., Wang, C., Kharel, P., Zhu, D. & Lončar, M. Integrated lithium niobate electro-optic modulators: When performance meets scalability. *Optica* **8**, 652–667 (2021).
30. Courjal, N., Bernal, M.-P., Caspar, A., Ulliac, G., Bassignot, F., Gauthier-Manuel, L., Suarez, M. Lithium niobate optical waveguides and microwaveguides, Emerging Waveguide Technology, 155 (2018).
31. Jelínková, H. et al. $LiNbO_3$ pockels cell for Q-switch of Er: YAG laser. *Laser Phys. Lett.* **1**, 59 (2004).
32. K.-K. Wong, Properties of Lithium Niobate, IET2002.
33. Easwaran, N., Balasubramanian, C., Narayandass, S. & Mangalaraj, D. Dielectric and AC conduction properties of thermally evaporated lithium niobate thin films. *Phys. Status Solidi (a)* **129**, 443–451 (1992).
34. Wang, B. et al. Atomic layer deposition of lithium niobium oxides as potential solid-state electrolytes for lithium-ion batteries. *ACS Appl. Mater. Interfaces* **10**, 1654–1661 (2018).
35. Lo Presti, F. et al. Malandrino, $LiNbO_3$ thin films through a sol–gel/spin-coating approach using a novel heterobimetallic lithium–niobium precursor. *Nanomaterials* **14**, 345 (2024).
36. Pellegrino, A. L. et al. Efficient optimization of high-quality epitaxial lithium niobate thin films by chemical beam vapor deposition: Impact of cationic stoichiometry. *Adv. Mater. Interfaces* **10**, 2300535 (2023).
37. Zivasatienraj, B., Tellekamp, M. B. & Doolittle, W. A. Epitaxy of $LiNbO_3$: Historical challenges and recent success. *Crystals* **11**, 397 (2021).
38. Tellekamp, M. B., Shank, J. C., Goorsky, M. S. & Doolittle, W. A. Molecular beam epitaxy growth of high crystalline quality $LiNbO_3$. *J. Electron. Mater.* **45**, 6292–6299 (2016).
39. Kilburger, S. et al. Growth of $LiNbO_3$ thin films on sapphire by pulsed-laser deposition for electro-optic modulators. *Appl. Surf. Sci.* **253**, 8263–8267 (2007).
40. Østreng, E., Sønsteby, H. H., Sajavaara, T., Nilsen, O. & Fjellvåg, H. Atomic layer deposition of ferroelectric $LiNbO_3$. *J. Mater. Chem. C* **1**, 4283–4290 (2013).
41. Zeng, X. et al. Morphology of lithium niobium oxide thin film ultrasonic transducers deposited by RF magnetron sputtering. *Ceram. Int.* **49**, 16297–16304 (2023).
42. Kalita, D., Lee, S., Lee, K., Ko, D. & Yoon, Y. Ionic conductivity properties of amorphous Li–La–Zr–O solid electrolyte for thin film batteries. *Solid State Ionics* **229**, 14–19 (2012).
43. Hallot, M., Roussel, P. & Lethien, C. Sputtered $LiNi_{0.5}Mn_{1.5}O_4$ thin films for lithium-ion microbatteries. *ACS Appl. Energy Mater.* **4**, 3101–3109 (2021).
44. Ferrari, V. C., Kim, N. S., Lee, S. B., Rubloff, G. W. & Stewart, D. M. Co-sputtering of lithium vanadium oxide thin films with variable lithium content to enable advanced solid-state batteries. *J. Mater. Chem. A* **10**, 12518–12531 (2022).
45. Jafarpour, S. & Naghshara, H. Reactive co-sputter deposition of Ta-doped tungsten oxide thin films for water splitting application. *Sci. Rep.* **15**, 8302 (2025).
46. Li, Q., Liu, W., Wang, J., Xia, Q. & Xia, H. Long-cycle-life Li_2MnO_3 thin-film cathode enabled by all-solid-state battery configuration. *J. Power Sources* **602**, 234371 (2024).
47. Jiang, M., Zhang, Q., Danilov, D. L., Eichel, R. D. A. & Notten, P. H. Formation of a stable solid-electrolyte interphase at metallic lithium anodes induced by $LiNbO_3$ protective layers. *ACS Appl. Energy Mater.* **4**, 10333–10343 (2021).
48. Lobe, S. et al. Radio frequency magnetron sputtering of $Li_7La_3Zr_2O_{12}$ thin films for solid-state batteries. *J. Power Sources* **307**, 684–689 (2016).
49. Jafarpour, S., Naghshara, H. & Parhizkar, M. The effect of DC power and annealing on the structural, optical, and electrical characteristics of sputtered amorphous WOX thin films. *Mater. Chem. Phys.* **313**, 128637 (2024).
50. Rahn, J. et al. Self-diffusion of lithium in amorphous lithium niobate layers. *Z. Phys. Chem.* **226**, 439–448 (2012).

51. Heitjans, P., Masoud, M., Feldhoff, A. & Wilkening, M. NMR and impedance studies of nanocrystalline and amorphous ion conductors: Lithium niobate as a model system. *Faraday Discuss.* **134**, 67–82 (2007).
52. Souquet, J. Ionic transport in amorphous solid electrolytes. *Annu. Rev. Mater. Sci.* **11**, 211–231 (1981).
53. Mazur, M. et al. Analysis of amorphous tungsten oxide thin films deposited by magnetron sputtering for application in transparent electronics. *Appl. Surf. Sci.* **570**, 151151 (2021).
54. Wang, B. et al. High-k gate dielectrics for emerging flexible and stretchable electronics. *Chem. Rev.* **118**, 5690–5754 (2018).
55. Li, S., Jiao, S., Wang, D., Gao, S. & Wang, J. The influence of sputtering power on the structural, morphological and optical properties of β-Ga_2O_3 thin films. *J. Alloys Compd.* **753**, 186–191 (2018).
56. Skryleva, E. et al. XPS study of Li/Nb ratio in $LiNbO_3$ crystals. Effect of polarity and mechanical processing on $LiNbO_3$ surface chemical composition. *Appl. Surface Sci.* **389**, 387–394 (2016).
57. Zhai, H. et al. The effects of Li/Nb ratio on the preparation and photocatalytic performance of Li–Nb–O compounds. *Nanoscale Res. Lett.* **12**, 496 (2017).
58. Kaufherr, N., Eichorst, D. & Payne, D. X-ray photoelectron spectroscopy studies of alkoxide-derived lithium niobate. *J. Vac. Sci. Technol. A: Vac. Surf. Films* **14**, 299–305 (1996).
59. Yang, H. & Wu, N. Ionic conductivity and ion transport mechanisms of solid-state lithium-ion battery electrolytes: A review. *Energy Sci. Eng.* **10**, 1643–1671 (2022).
60. Jonscher, A. K. The 'universal'dielectric response. *Nature* **267**, 673–679 (1977).
61. Mahler, J. & Persson, I. A study of the hydration of the alkali metal ions in aqueous solution. *Inorg. Chem.* **51**, 425–438 (2012).
62. Yao, G. et al. Structure, chemical bond and microwave dielectric characteristics of novel $Li_3Mg_4NbO_8$ ceramics. *J. Eur. Ceram. Soc.* **41**, 6490–6494 (2021).
63. Meesala, Y. et al. An efficient multi-doping strategy to enhance Li-ion conductivity in the garnet-type solid electrolyte $Li_7La_3Zr_2O_{12}$. *J. Mater. Chem. A* **7**, 8589–8601 (2019).
64. Lin, F., Wang, Y. & Lonergan, M. Ion transport in polyacetylene ionomers. *J. Appl. Phys.* **104**, 103517 (2008).
65. Jafarpour, S., Naghshara, H. & Aslibeiki, B. Correlation of sputtering power with microstructure and ionic conductivity in lithium aluminum oxide thin films prepared by reactive co-sputtering. *Ceram. Int.* **50**, 5665–5675 (2024).
66. Clayton, D. R., Lepage, D., Woods, K. N., Page, C. J. & Lonergan, M. C. Solution-processed Li_2O–Al_2O_3/TiO_2 nanolaminate stacks containing mobile lithium ions and with increased breakdown voltages. *ACS Appl. Mater. Interfaces* **12**, 1241–1249 (2019).
67. Bharti, D. C. & Rhee, S.-W. Dielectric properties and X-ray photoelectron spectroscopic studies of niobium oxide thin films prepared by direct liquid injection chemical vapor deposition method. *Thin Solid Films* **548**, 195–201 (2013).
68. Pal, N. et al. Gate interface engineering for subvolt metal oxide transistor fabrication by using ion-conducting dielectric with Mn_2O_3 gate interface. *ACS Appl. Electron. Mater.* **2**, 25–34 (2019).
69. Jonscher, A. Physical basis of dielectric loss. *Nature* **253**, 717–719 (1975).
70. Arya, A. & Sharma, A. L. Effect of salt concentration on dielectric properties of Li-ion conducting blend polymer electrolytes. *J. Mater. Sci.: Mater. Electron.* **29**, 17903–17920 (2018).
71. Hu, Y. et al. Electrical characterization of amorphous $LiAlO_2$ thin films deposited by atomic layer deposition. *RSC Adv.* **6**, 60479–60486 (2016).
72. Wang, Q. & Liu, Q. Enhancement of ionic conductivity and air stability by co-doping $Li_{10}SnP_2S_{12}$ with Nb and O. *J. Energy Storage* **104**, 114505 (2024).
73. Glass, A., Nassau, K. & Negran, T. Ionic conductivity of quenched alkali niobate and tantalate glasses. *J. Appl. Phys.* **49**, 4808–4811 (1978).
74. Benaissa, K., Ashrit, P., Bader, G., Girouard, F. E. & Truong, V.-V. Electrical and optical properties of $LiNbO_3$. *Thin Solid Films* **214**, 219–222 (1992).
75. Can, N., Ashrit, P., Bader, G., Girouard, F. & Truong, V. V. Electrical and optical properties of Li-doped $LiBO_2$ and $LiNbO_3$ films. *J. Appl. Phys.* **76**, 4327–4331 (1994).
76. Xia, H., Wang, H. L., Xiao, W., Lai, M. O. & Lu, L. Thin film Li electrolytes for all-solid-state micro-batteries. *Int. J. Surf. Sci. Eng.* **3**, 23–43 (2009).
77. Ito, Y. & Tsuyumoto, I. Preparation of nanocrystalline $LiNbO_3$ through aqueous solution process using peroxo-polyniobic acid. *Mater. Chem. Phys.* **272**, 125035 (2021).
78. Özer, N. & Lampert, C. M. Electrochemical lithium insertion in sol–gel deposited $LiNbO_3$ films. *Sol. Energy Mater. Sol. Cells* **39**, 367–375 (1995).
79. Joshi, V., Roy, D. & Mecartney, M. Low temperature synthesis and properties of lithium niobate thin films. *Appl. Phys. Lett.* **63**, 1331–1333 (1993).
80. Rost, T. A., Lin, H., Rabson, T. A., Baumann, R. C. & Callahan, D. L. Deposition and analysis of lithium niobate and other lithium niobium oxides by rf magnetron sputtering. *J. Appl. Phys.* **72**, 4336–4343 (1992).

Acknowledgements
This project is supported by the research grant of the University of Tabriz (number SAD/3881-1402/12/26).

Author contributions
A.B. Samaneh Jafarpour wrote the main manuscriptA.B. Hamid Naghshara wrote the main manuscriptE.F. Hamaneh Zarenezhad performed the XPS analysis.

Funding
No funding required.

Declarations

Competing interests
The authors declare no competing interests.

Additional information
Correspondence and requests for materials should be addressed to H.N.

Reprints and permissions information is available at www.nature.com/reprints.

Publisher's note Springer Nature remains neutral with regard to jurisdictional claims in published maps and institutional affiliations.

Open Access This article is licensed under a Creative Commons Attribution-NonCommercial-NoDerivatives 4.0 International License, which permits any non-commercial use, sharing, distribution and reproduction in any medium or format, as long as you give appropriate credit to the original author(s) and the source, provide a link to the Creative Commons licence, and indicate if you modified the licensed material. You do not have permission under this licence to share adapted material derived from this article or parts of it. The images or other third party material in this article are included in the article's Creative Commons licence, unless indicated otherwise in a credit line to the material. If material is not included in the article's Creative Commons licence and your intended use is not permitted by statutory regulation or exceeds the permitted use, you will need to obtain permission directly from the copyright holder. To view a copy of this licence, visit http://creativecommons.org/licenses/by-nc-nd/4.0/.

© The Author(s) 2025